

Transmission across a bilayer graphene region

Hadi Z. Olyaei¹, Pedro Ribeiro^{1,2}, Eduardo V. Castro^{1,2,3}

¹*CeFEMA, Instituto Superior Técnico, Universidade de Lisboa, Av. Rovisco Pais, 1049-001 Lisboa, Portugal*

²*Beijing Computational Science Research Center, Beijing 100084, China and*

³*Centro de Física das Universidades do Minho e Porto,
Departamento de Física e Astronomia, Faculdade de Ciências,
Universidade do Porto, 4169-007 Porto, Portugal*

The transmission across a graphene bilayer region is calculated for two different types of connections to monolayer leads. A transfer matrix algorithm based on a tight binding model is developed to obtain the ballistic transmission beyond linear response. The two configurations are found to behave similarly when no gate voltage is applied. For a finite gate voltage, both develop a conductance gap characteristic of a biased bilayer, but only one shows a pronounced conductance step at the gap edge. A gate voltage domain wall applied to the bilayer region renders the conductance of the two configurations similar. For a microstructure consisting of equally spaced domain walls, we find a high sensitivity to the domain size. This is attributed to the presence of topologically protected in-gap states localized at domain walls, which hybridize as the domain size becomes of the order of their confining scale. Our results show that transmission through a bilayer region can be manipulated by a gate voltage in ways not previously anticipated.

I. INTRODUCTION

The unique band structure of graphene gives rise to several alluring phenomena which have been the subject of intense research since its experimental discovery in 2004 [1–4]. In particular, its high charge-carrier mobility has rendered graphene a highly attractive and promising component for electronic and optoelectronic devices [5, 6]. Another appealing feature of graphene for device application is its stability at the nanometer scale, ensured by the covalent bonds among the carbon atoms [7], which is highly desirable for device-miniaturization. A graphene-based electronic device, entirely made out of micro-structured graphene sheets, is thus expected to reduce significantly energy dissipation and optimize device-miniaturization and functionality [8–10]. The recent realization of a short channel field-effect transistor, using just 9- and 13-atom wide graphene nanoribbons [11], is a convincing step in that direction. This is to be contrasted with mainstream semiconductor technology which usually integrates different materials and where component-interfacing can be difficult to scale-down [12].

Although a gapless conductor, the versatility of the electronic properties of graphene make it possible to easily induce a gap. This can be done by several means: cutting it into nanoribbons with zigzag or armchair edges [13–16]; by breaking inversion symmetry with an appropriate substrate [17]; or applying an out-of-plane electric field in graphene bilayer structures [18–21].

Compared to monolayer graphene, the possibility of tuning the induced gap by an external, perpendicular electrical field, which is easily introduced through a gate potential, makes the bilayer more suitable to device applications [22]. Not only the gap can be tuned by a gate bias, but also a twist angle can be engineered between the two layers [23, 24]. This leads to a strong reconstruction

of the band structure at low energies [25]. The recent observation of superconductivity and insulating behavior in twisted bilayer graphene at the magic angles clearly shows the high degree of tunability of this system [26, 27]. Further manipulation of the bilayer response is possible by inserting an insulator between the two graphene layers, out of which tunnel field effect transistors have been realized [9, 28–32].

One other advantage of the graphene bilayer is that its electronic structure can be manipulated by a layer-selective potential, induced by a gate voltage. The possibility of sharply reversing the sign of voltage, thus creating a well-defined one-dimensional boundary separating regions of constant potential, has been demonstrated recently [33]. These domain walls support confined one-dimensional states that are topologically protected and can be used as purely one-dimensional channels [34, 35].

The ballistic transport across a bilayer graphene region has been studied at length [36–42]. Particular attention has been given to a setup where a gate voltage is applied within the bilayer region [37, 38, 41, 42]. These studies already revealed a high degree of tunability of the transport properties. However, the effects of further manipulations of the gate voltage, namely through the creation of a domain wall affecting the bilayer region [33] are yet to be investigated. Furthermore, the possibility of a microstructured gate voltage with several built-in domain walls opens up new avenues to engineer electronic transport at the nanoscale.

The aim of this paper is to study ballistic transport of micro-structured bilayer graphene flakes of with different types of connection to monolayer. Using a tight-binding model of an AB stacked bilayer flake, taken to be infinite in the transverse direction, we observe that the conductance displays aperiodic oscillations as a function of chemical potential. The conductance in the presence

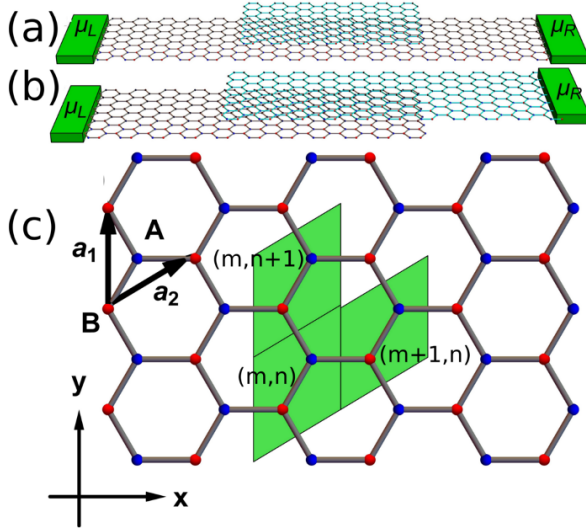


FIG. 1. System setups with a bilayer region used in this work: (a) the $1 \rightarrow 1$ setup; (b) the $1 \rightarrow 2$ setup. (c) Primitive vectors \mathbf{a}_1 and \mathbf{a}_2 , sublattice labels A (blue) and B (red), and unit cell labeling of the monolayer structure.

of a single voltage domain is shown to be compatible with previous results obtained within a low energy approximation. We compute the conductance in the presence of a domain wall in the gate bias and show that, in this case, geometries with different types of connection to monolayer leads behave similarly. We further study the effect of a micro-structured gate bias with multiple domain walls. By changing the separation between domain-walls we explore the crossover from well separated domain-wall states to the fully hybridized regime where in-gap states start to contribute to the conductance. Finally, we have studied the viability of an integrated nano-transistor for experimentally reasonable conditions finding that this setup can achieve on/off ratios of the output current within $50 \lesssim I_{\text{on}}/I_{\text{off}} \lesssim 200$.

The structure of the paper is as follows: in Sec. II, we introduce the model of the physical setup and the corresponding tight-binding formulation as well as the method for obtaining the transmission across the bilayer region using the transfer matrix formulation. In Sec. III, some representative results of transmission are presented, including the new types of micro-structured gated bilayer graphene. Sec. IV contains a short summary and the conclusions. In Sec. A, we present some of the details of the calculation of the transmission.

II. MODEL AND METHODS

Schematics of the setup for which the transmission and the conductance are studied is shown in Fig. (1). The case of Fig. 1(a) consists of a single layer of graphene with a flake of another layer on top, the $1 \rightarrow 1$ setup. The sec-

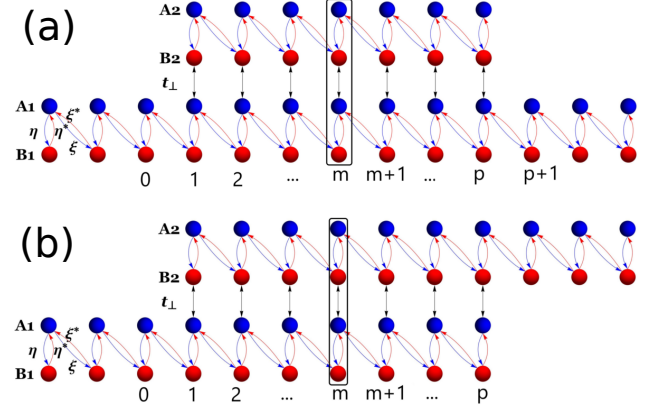


FIG. 2. 1D effective chain obtained after Fourier transform, as described in the main text: (a) The $1 \rightarrow 1$ configuration; (b) the $1 \rightarrow 2$ configuration.

ond configuration is obtained from two sheets of graphene that are partially overlapped, the $1 \rightarrow 2$ setup, as shown in Fig. 1(b). In both we consider A-B stacking. Translational invariance along the transverse direction (y axis) is presumed. We are interested in the ballistic regime where the electronic mean free path is larger than the typical length of the device. For simplicity we consider the case of perfect contacts, which can be replaced by infinite leads.

We model electrons in the structure using the conventional tight-binding approach for p_z -electrons [4] hopping between nearest neighbor carbon sites of the atomic lattice shown in Fig. (1)(c), which can be written as $H = H_1 + H_2 + H_\perp$. Here,

$$H_j = -t \sum_{m,n} a_{j,m,n}^\dagger [b_{j,m,n} + b_{j,m+1,n} + b_{j,m,n+1}] \quad (1)$$

$$+ \sum_{m,n \in \text{BL}} V_j [a_{j,m,n}^\dagger a_{j,m,n} + b_{j,m,n}^\dagger b_{j,m,n}] + h.c \quad (2)$$

is the Hamiltonian of the $j = 1, 2$ layer, and

$$H_\perp = -t_\perp \sum_{m,n \in \text{BL}} a_{1,m,n}^\dagger b_{2,m,n} + h.c. \quad (3)$$

is the inter-layer hopping term, with a_j^\dagger (b_j^\dagger) the creation operators of a particle in sublattice A (B) in the (m, n) unit cell of the j th layer. The effect of an applied gate voltage within the bilayer region is modeled by V_j . The BL restriction in the summation stands for sites belonging to the bilayer region.

After Fourier transformation in the y -direction, the stationary states of the 1D effective chain for the two cases shown in Fig. (2) can be written as

$$|\psi_k\rangle = \sum_{j=1,2} \sum_m \left(\psi_{m,k}^{A,j} a_{j,m,k}^\dagger + \psi_{m,k}^{B,j} b_{j,m,k}^\dagger \right) |0\rangle, \quad (4)$$

with k the wave number along the y direction. Within the monolayer (lead) region, we define the column vector $\Psi_k^j(m) = \left[\psi_{m-1,k}^{A,j}, \psi_{m,k}^{B,j} \right]^T$ which obeys the transfer matrix equation (see Appendix A),

$$\Psi_k^{1(2)}(m+1) = \mathbb{T}_L \Psi_k^{1(2)}(m), \quad (5)$$

where \mathbb{T}_L is given by

$$\mathbb{T}_L = \frac{1}{\xi \eta^*} \begin{bmatrix} -|\xi|^2 & -\epsilon \xi \\ \epsilon \xi^* & \epsilon^2 - |\eta|^2 \end{bmatrix}, \quad (6)$$

with $\eta = t(1 + e^{ik})$ and $\xi_k = t$. For the bilayer region ($1 \leq m \leq p$) we define $\Psi_k(m) = \left[\Psi_k^1(m), \Psi_k^2(m) \right]^T$ obeying

$$\Psi_k(m+1) = \mathbb{T}_{BL} \Psi_k(m), \quad (7)$$

where the transfer matrix \mathbb{T}_{BL} is given by

$$\mathbb{T}_{BL} = \frac{1}{\eta^* \xi} \begin{bmatrix} -|\eta|^2 & -\epsilon \eta & 0 & 0 \\ \epsilon \eta^* & \epsilon^2 - |\xi|^2 & 0 & -t_\perp \\ t_\perp \frac{|\eta|^2}{\xi^*} & t_\perp \frac{\epsilon \eta}{\xi^*} & -|\eta|^2 & -\epsilon \eta \\ -t_\perp \frac{\epsilon \eta^*}{\xi^*} & -t_\perp \frac{\epsilon^2}{\xi^*} & \epsilon \eta^* & \epsilon^2 - |\xi|^2 \end{bmatrix}. \quad (8)$$

The amplitudes at the left and the right interfaces can be related by,

$$\Psi_k(p+1) = (\mathbb{T}_{BL})^p \Psi_k(1) \quad (9)$$

and by the boundary conditions: $\psi_{0,k}^{A2} = \psi_{p+1,k}^{B2} = 0$ for the $1 \rightarrow 1$ case, and $\psi_{0,k}^{A2} = \psi_{p+1,k}^{B1} = 0$ for the $1 \rightarrow 2$ case, as can be seen in Figs. 2(a) and 2(b). With these boundary conditions one obtains the matrix $\mathcal{M}_{1 \rightarrow 1(2)}$ relating the layer 1 in the left to layer 1(2) in the right,

$$\Psi_k^{1(2)}(p+1) = \mathcal{M}_{1 \rightarrow 1(2)} \Psi_k^1(1), \quad (10)$$

where $\mathcal{M}_{1 \rightarrow 1(2)}$ are defined from Eq. (9) in Appendix A.

Within the semi-infinite leads, Eq. (5) can be solved by assuming the ansatz

$$\Psi_k^{1(2)}(m) = \alpha_+ \lambda_+^{m-1} \zeta_k^+ + \alpha_- \lambda_-^{m-1} \zeta_k^-,$$

with $\mathbb{T}_L \zeta_k^\pm = \lambda_\pm \zeta_k^\pm$. The eigenvalues λ_\pm and the eigenmodes ζ_k^\pm are explicitly derived in Appendix A. In the leads we only consider propagating modes, so that

$|\lambda| = 1$. The eigenmodes are thus interpreted as left-moving, ζ_j^- , and right-moving, ζ_j^+ , modes, according to their group velocity (see Appendix A). We then use the ζ_k^\pm eigenbasis to write the wave function in the leads,

$$\Psi_k^{1(2)}(m) = \lambda_+^{m-1} \zeta_k^+ + \lambda_-^{m-1} r_k \zeta_k^- \quad , \quad m < 1 \quad (11)$$

$$\Psi_k^{1(2)}(m) = \lambda_+^{m-p-1} \tau_k \zeta_k^+ \quad , \quad m > p, \quad (12)$$

from which we define transmission and reflection coefficients, respectively τ and r . The transmission and reflection coefficients are given by,

$$\begin{bmatrix} \tau_k \\ 0 \end{bmatrix} = U^{-1} \mathcal{M}_{1 \rightarrow 1(2)} U \begin{bmatrix} 1 \\ r_k \end{bmatrix}, \quad (13)$$

where $U = \left[\zeta_k^+, \zeta_k^- \right]$.

The transmission probability is then defined as $T(\epsilon, k) = 1 - |r_k|^2 = |\tau_k|^2$, and the overall transmission per transverse unit length is given by,

$$\bar{T}(\epsilon) = \frac{1}{2\pi} \int_{-\pi}^{\pi} dk T(\epsilon, k). \quad (14)$$

Using the Landauer formula [43], we find the current per transverse unit length across the bilayer region,

$$I = \frac{2e}{h} \int d\epsilon \bar{T}(\epsilon) [f(\epsilon - \mu_L) - f(\epsilon - \mu_R)] \quad (15)$$

where $f(\epsilon)$ is the Fermi distribution function and $\mu_L(\mu_R)$ are the chemical potential in the left (right) lead (in the following we assume $\mu_L > \mu_R$). Assuming $\mu \equiv \mu_L = \mu_R + \delta\mu$, with $\delta\mu \ll \mu$, we can linearize the Landauer formula [44] to obtain the conductance $G \equiv e\delta I/\delta\mu$, which can be written as

$$G(\mu) = -G_0 \int d\epsilon T(\epsilon) \frac{\partial f(\epsilon - \mu)}{\partial \epsilon}, \quad (16)$$

where $G_0 = \frac{2e^2}{h}$ is the conductance quantum. For a system at zero temperature, Eq. (16) can be simplified to $G = G_0 T(\mu)$.

III. RESULTS AND DISCUSSION

A. Transmission through a bilayer graphene region

In this section, we compute the transmission amplitudes for the $1 \rightarrow 1$ and $1 \rightarrow 2$ cases. A simplifying feature is that, for both cases, there is only one propagating incident mode associated with given ϵ , hence the

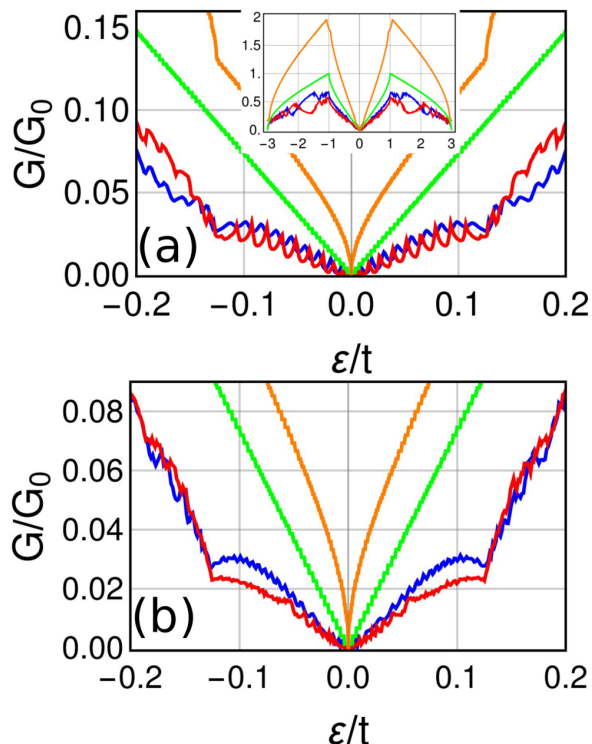


FIG. 3. Transmission per transverse unit length near the Fermi-level for the $1 \rightarrow 1$ (blue), $1 \rightarrow 2$ (red) geometries plotted for $p = 200$ (a) and $p = 1500$ (b). The transmission for an infinite graphene layer (green) and for an infinite bilayer (orange) are plotted for comparison. Inset: Transmission for the whole bandwidth for $p = 200$.

corresponding transfer matrix of the leads is a two by two. Note that, due to electron-hole symmetry, $T(\epsilon, k) = T(\pm\epsilon, k)$.

Figure 3 shows the conductance for energies near the Fermi-level for the $1 \rightarrow 1$ (blue) and $1 \rightarrow 2$ (red) geometries and for two values of the scattering region size, $p = 200$, (a), and for $p = 1500$, (b). For comparison, the conductance through an infinite system consisting of a single (green) or a double (orange) graphene layer is also depicted. Note that, in these cases the total transmission in Eq. (14) is simply determined by the dispersion relation. Therefore, for low energies it behaves as $\propto |\epsilon|$ for the single layer and as $\propto |\epsilon|^{1/2}$ for the bilayer.

For both geometries, the low energy conductance is almost twice as low as for pristine graphene and vanishes faster, with a $\propto |\epsilon|^2$ scaling behavior. The inset of Fig. 3(a), depicting G for the all energies within the bandwidth, shows that, even away from the Fermi-level, G never attains the value of the pristine case.

Another pronounced low energy feature of the transmission, is the sudden increase for energies around t_{\perp} . Thus, as also seen in the pristine double layer case, the conductance resolves the appearance of the higher energy band, after which two propagating modes become

available for transport within the bilayer region.

The differences between the $1 \rightarrow 1$ and $1 \rightarrow 2$ geometries are more pronounced for higher energies. At low energies, they can be completely masked out by the finite-size effects that yield the characteristic jumps in the conductance, Fig. 3(a). For larger values of p , when the finite-size oscillations are reduced, the $1 \rightarrow 1$ case is seen to have a higher conductance. This is to be expected since in this case the transmitted electrons do not have to change layer, which is suppressed for low values of t_{\perp} .

B. Conductance through a *gated* bilayer graphene region

1. Homogeneous case

In this section, we study the effect on the transmission of a gate voltage applied within the bilayer region. We assume that only one of the layers is affected by the gate while the other remains at zero voltage. We study the cases for which the voltage of the lower, V_1 , or upper layers, V_2 , is $0.04t$ or ten times larger $0.4t$, which correspond to typical values of gate voltages that can be implemented experimentally.

Fig. 4 shows the conductance through a gated bilayer graphene region in different cases together with a plot of the band structure of the bilayer and the single layer leads around zero energy (computed assuming an infinite system).

Fig. 4(b) depicts the $1 \rightarrow 1$ geometry for $V_1 = 0.04t$ and $V_2 = 0$ (blue) and for the swapped voltage configuration $V_1 = 0$ and $V_2 = 0.04t$ (green). The most pronounced features are the suppression of transport for $\epsilon \in \{0, |\Delta V|\}$ and a jump in the conductance for $\epsilon \approx |\Delta V|$ seen in 4(b) blue, which is not present when the gate voltages are swapped in 4(b) (green). The illustrations of the band structures in Figs. 4(a) and 4(c) help to understand this behavior. The effect of the gate voltage is to open up a gap in the dispersion relation of the bilayer. Moreover, while for $V_1 = V_2 = 0$, the wavefunction's amplitudes are equally distributed between the two layers of the bilayer system, for finite voltages their distribution changes drastically near the gap edges (valence band maximum and conduction band minimum). The color coding in Fig. 4(a) and 4(c) shows the localization of the wave-function in the upper or lower layers. This energy-dependent layer distribution can simply explain the conduction jump: in the case depicted in 4(a), after passing the energy gap the system has suddenly available a large density of transmission modes within the lower layer. Such matching conditions (same color, at a given energy, for the leads and the bilayer region) never arises in the opposite case, 4(b) green, as can be seen in 4(c).

Figs. 4(e) depicts the transmission for the $1 \rightarrow 2$ ge-

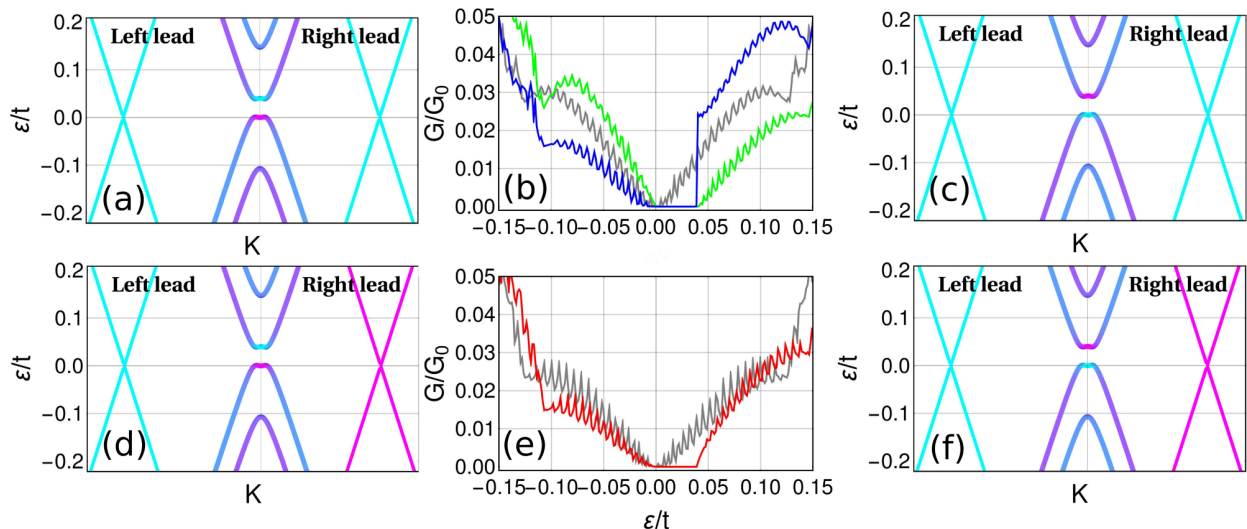


FIG. 4. Conductance for a gated bilayer region. Upper panels refer to the geometry $1 \rightarrow 1$ (a-c) and lower panels to $1 \rightarrow 2$ (d-f). (b) Blue and (e) red correspond to $V_1 = 0.04t$ and $V_2 = 0$, computed for $p = 400$. For (b) green and (e) red: the values of the voltage are swapped, i.e. $V_1 = 0$ and $V_2 = 0.04t$. Notice that the geometry $1 \rightarrow 2$ is unchanged under swapping the gate voltage. The unbiased case $V_1 = V_2 = 0$ is depicted as a gray line for comparison. The dispersion relations at low energies, computed for an infinite system, corresponding respectively to the setups (b) blue, (b) green, and (e) red are given in (a), (c), (d) and (f). The central dispersion corresponds to the bilayer region and the color encodes whether the wave-function is localized in the bottom (cyan) or in the upper (pink) layers. The left and right dispersions correspond to a single layer and follow the same color coding.

ometry. This case is symmetric under the swapping of the voltages. In this case Figs. 4(d) and 4(f) show that the perfect matching conditions seen in 4(a) are never attained and thus no jump in conductance is observed.

The conductance attained when the gate voltage is increased by one order of magnitude is depicted in Fig. 5(a) for the two geometries $1 \rightarrow 1$ (blue) and $1 \rightarrow 2$ (red) for $V_1 = 0.4t$ and $V_2 = 0$. The inset shows the voltage swapped case, $V_1 = 0$ and $V_2 = 0.4t$. Fig. 5(b) depicts the band structure, with the same color coding as before, corresponding to the case $1 \rightarrow 1$ and $V_1 = 0.4t$ and $V_2 = 0$. An interesting feature of the transmission in Fig. 5(a) is that there are two regions where the conduction seems to vanish. One, at higher energies, corresponds to the band-gap and thus the suppression of the conductance is not surprising. However, the second arises within a region where the density of states is finite. Again, the plot of the band structure in Fig. 5(b) can simply explain this effect: the gap in conductance corresponds to a region where the conducting states with support on the lower layer become gapped, so although the total density of states is finite, there are no states contributing to transport.

2. Inhomogeneous case: single domain wall

In this section, we study how the transmission is affected by the presence of an inhomogeneous gate volt-

age. We consider the simplest case where a gate voltage domain wall is present in the bilayer region. We assume that the local potential at cell m , layer j (see Fig. 2) is given by $V_{m,j} = V_0 \Theta \left[(-1)^j \left(m - \frac{p}{2} \right) \right]$, with $\Theta(x)$ the Heaviside function. Therefore, the potential difference on the left half ($m < p/2$) is $V_1 - V_2 = V_0$ while on the right half ($m > p/2$) it is $V_1 - V_2 = -V_0$, which implies a domain wall right at the middle of the bilayer region. This domain wall structure is known to support confined states, localized in the transverse direction and extending along the wall [34], with important consequences regarding transport in the direction of the wall [33]. The impact of a domain wall on charge transport in the perpendicular direction has not been studied before and is analyzed in the following.

In Fig. 6 we show the conductance for the geometries $1 \rightarrow 1$ (blue) and $1 \rightarrow 2$ (red) for $V_0 = 0.04t$. The two geometries now have very similar conductance, which contrasts with the case when no domain wall is present, depicted in Figs. 4(b) and 4(f). A noticeable difference is the absence of the jump in conductance observed for the $1 \rightarrow 1$ geometry in Fig. 4(b). Since the domain wall reverses the layer distribution of the wave-function's amplitudes, the perfect matching conditions seen in 4(a) are never attained and thus no jump in conductance is observed. We conclude that the domain wall erases the difference between the two geometries.

As shown in Ref. [34], the states confined at the domain wall originate one-dimensional bands dispersing in-

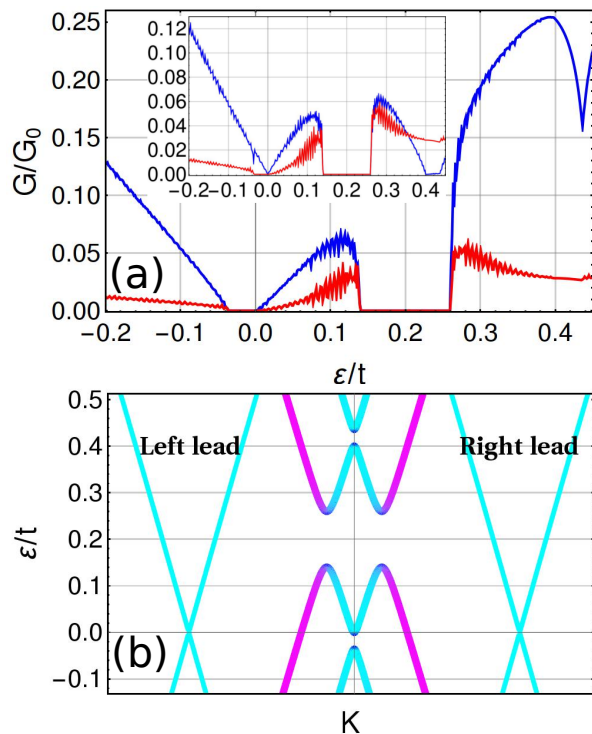


FIG. 5. (a) Conductance for the a gated bilayer region computed for $p = 400$ for the $1 \rightarrow 1$ (blue) and $1 \rightarrow 2$ (red) geometries with $V_1 = 0.4t$ and $V_2 = 0$. The inset depict the opposite voltage configuration: $V_1 = 0$ and $V_2 = 0.4t$. (b) The dispersion relations at low energies, computed for an infinite system, corresponding to the setup (a). The central dispersion corresponds to the bilayer region and the color encodes whether the wave-function is localized in the bottom (cyan) or in the upper (pink) layers. The left and right dispersions correspond to a single layer and follow the same color coding.

side the bulk gap. In Fig. 6 the impact of those states is unnoticeable, as a well resolved gap of order $\sim V_0$ is still apparent. This can be understood as a consequence of transverse confinement. At low energies, the wave function of these states has a decay length of the order $\beta \approx a_0 t / \sqrt{V_0 t_{\perp}} \gg a_0$, where a_0 is the carbon-carbon distance [34]. For $V_0 = 0.04t$ the decay length is $\beta \approx 8a_0$, much smaller than the distance $l = 200a_0$ between the domain wall and the edges of the scattering region. Therefore, for a single domain wall, these states do not contribute to propagate charge across the bilayer region.

C. Conductance through a *microstructured* biased bilayer graphene region

We now generalize our study to multiple domain walls. Our aim is to show how these microstructures, that are now routinely fabricated, can be used to engineer the transmission. We consider the potential of the previous

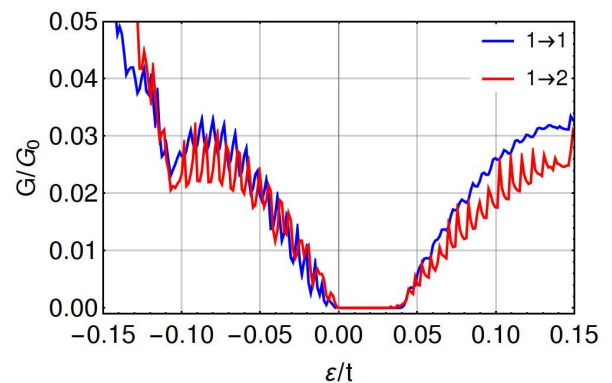


FIG. 6. Conductance for the a bilayer region with a gate voltage domain wall in the middle, computed for $p = 400$ in the $1 \rightarrow 1$ (blue) and $1 \rightarrow 2$ (red) geometries with $V_0 = 0.04t$.

section generalized for a periodic gated region of size l , $V_{m,1} = V_0 \Theta_l[m]$, where

$$\Theta_l[m] = \begin{cases} 1 & \text{if } 2kl/a_0 < m < (2k+1)l/a_0 \text{ for } k \in \mathbb{Z} \\ 0 & \text{if else} \end{cases},$$

and $V_{m,2} = V_0 (1 - \Theta_l[m])$. As a function of l , there are two qualitatively different cases that we consider in the following: a large domain length, $l \gg \beta$, where the edge modes along the domain wall do not hybridize and thus do not contribute to the transport properties; and a small domain length, $l \lesssim \beta$, for which there is hybridization of edge modes and thus transport for energies within the bulk gap becomes possible.

Figure 7 shows the evolution of the conductance curves with l . We consider, as before, $V_0 = 0.04t$ corresponding to $\beta \approx 8a_0$. In Fig. 7(a) we show the conductance for $l = 80a_0 \gg \beta$. As for the $l = p/2$ case in the previous section, the differences between the two geometries are not significant and there is almost no conductance within the gap, for $\varepsilon \in \{0, V_0\}$.

Figure 7(b) depicts the conductance for a smaller value of $l = 20a_0$. Here, there are already some states within the gap that contribute to transport which result from the hybridization of the edge modes along the domain walls.

In Fig. 7(c) we set $l = 5a_0$, for which the domain wall states are already fully hybridized. Note the striking similarity between the low energy conductance and that obtained for an unbiased bilayer region, shown in Fig. 3 and as a background in Figs. 4(b-c) and 4(f-g). It is clear that the effect of the gap has been completely washed out. At higher energies, however, the system still shows the conductance asymmetry typical of a gate biased bilayer region [see Figs. 4(b-c) and 4(f-g)].

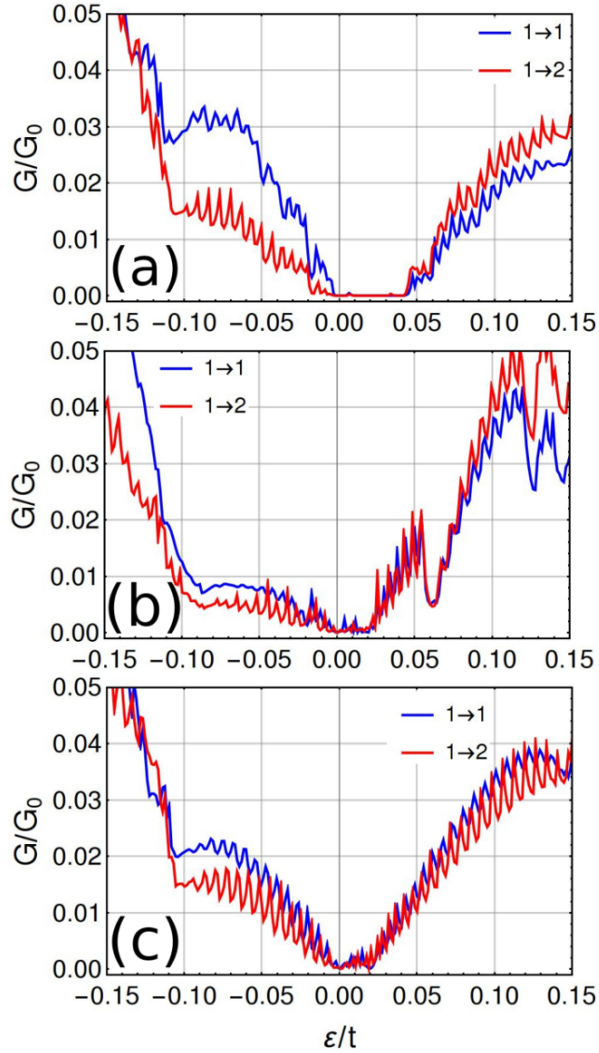


FIG. 7. Conductance for the $1 \rightarrow 1$ (Blue) and the $1 \rightarrow 2$ (red) geometries in the presence of multiple domain walls separated by l lattice spacings, computed for $V_0 = 0.04t$. (a) $l = 80a_0 \gg \xi$. (b) $l = 20a_0 > \xi$. (c) $l = 5a_0 \approx \xi$.

D. Results for current at finite temperature and device application

In this section, we study the viability of an integrated nano-transistor based on the $1 \rightarrow 1$ or $1 \rightarrow 2$ geometries.

For this device, one aims to maximize the current ratio between the “on” and “off” currents, I_{on} and I_{off} , passing through the terminals, when changing between two values of the applied gate voltage. Due to its low resistance and versatility, graphene is a natural candidate for transistor implementations. However, due to the nature of its band structure, achieving a high on/off ratio is a technical challenge specially at finite temperature. We exploit the non-linear behavior of the conductance obtained with the setup of Fig. 4(b) to optimize the $I_{\text{on}}/I_{\text{off}}$ and study its behavior at finite temperature.

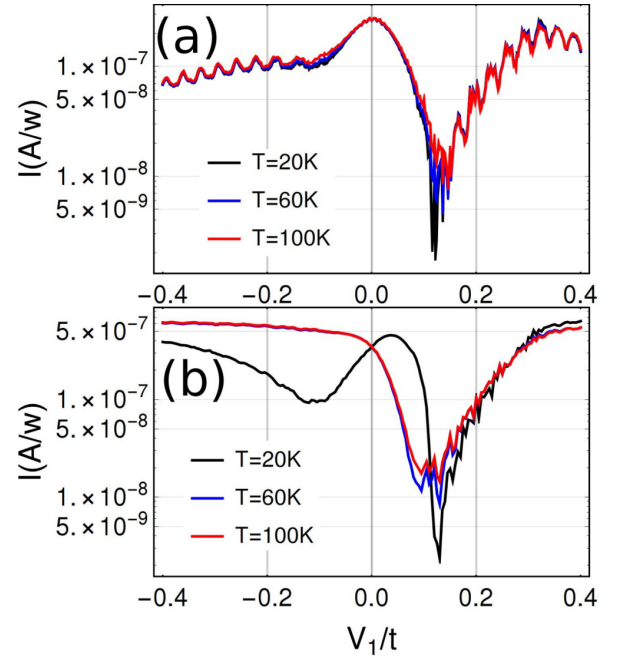


FIG. 8. Current as a function of gate voltage for the setup of Fig. 4(b) as a function of V_1 (for $V_2 = 0$) computed for $p = 200$ and different values of the temperature for the $1 \rightarrow 1$ (a) and $1 \rightarrow 2$ (b) geometries.

Figure (8) shows the logarithmic plot of the current for the $1 \rightarrow 1$, panel (8)(a), and $1 \rightarrow 2$, panel (8)(b), setups for different temperatures as a function of gate voltage V_1 . The chemical potentials on the left and right leads were fixed at the experimentally reasonable values of $\mu_L = 0.1t$ and $\mu_R = 0$. In the gate voltage interval $0 < V_1 < 0.2t$ this setup can achieve $50 \lesssim I_{\text{on}}/I_{\text{off}} \lesssim 200$.

IV. CONCLUSION

In this work, we have studied the conductance across a graphene bilayer region for two different positions of the single layer leads: the case when the leads connect to the same layer, the $1 \rightarrow 1$ configuration; and the case when the leads connect to different layer, $1 \rightarrow 2$ configuration. We have worked in the limit of an infinitely wide scattering region, to avoid edge effects, and developed a transfer matrix, tight-binding based methodology which allows to go away from linear response. We have found that, when there is no gate bias applied to the bilayer region, the two setups, $1 \rightarrow 1$ and $1 \rightarrow 2$, have a similar behavior, with a slightly higher conductance in the $1 \rightarrow 1$ configuration. The presence of a bias gate voltage differentiates between the two configurations. Both of them develop a conductance gap which mimics the spectral gap of a biased bilayer, but only the $1 \rightarrow 1$ configuration shows a pronounced conductance step at one of the gap edges, extending the results obtained in the

continuum limit [37] and for ribbons of finite width [41]. This step is not present if the gate polarity is reversed. Introducing a domain wall in the gate bias applied to the bilayer region, the conductance step disappears and the two configurations, $1 \rightarrow 1$ and $1 \rightarrow 2$, behave again in a similar way.

We have also studied the effect of a gate bias with a multiple domain wall microstructure applied to the bilayer region. When the separation between domains is much larger than the localization length of the states confined at the domain walls, the multiple domain walls states behave independently and the result is similar to the case of a single domain wall. On decreasing the separation between domain walls, the localized states start to hybridize and a finite conductance starts to appear inside the gap. At even smaller distances, the gap is completely washed out, and only at higher energies a conductance asymmetry characteristic of a gate biased bilayer region is present. Finally, we have studied the viability of an integrated nano-transistor based on the $1 \rightarrow 1$ or $1 \rightarrow 2$ geometries. For experimentally reasonable chemical potential difference (~ 0.3 eV) and gate voltage interval (from 0 up to ~ 0.6 eV) we have found that this setup can achieve $50 \lesssim I_{\text{on}}/I_{\text{off}} \lesssim 200$. Summing up all the finds, it is clear the transmission through a bilayer region can be manipulated by a gate bias in ways not previously anticipated.

We thank B. Amorim for valuable discussions. The authors acknowledge partial support from FCT-Portugal through Grant No. UID/CTM/04540/2013. H.Z.O acknowledges the support from the DP-PMI and FCT (Portugal) through scholarship PD/BD/113649/2015. PR acknowledges support by FCT-Portugal through the Investigador FCT contract IF/00347/2014.

Appendix A: The transmission through a bilayer region

Here we detail the transfer matrix method used to obtain the transmission coefficient. We apply Fourier transformation,

$$a_{j,m,k}^\dagger (b_{j,m,k}^\dagger) = \frac{1}{\sqrt{N_y}} \sum_n \exp(ikn) a_{j,m,n}^\dagger (b_{j,m,n}^\dagger),$$

to the tight-binding Hamiltonian (1) and obtain

$$\begin{aligned} H_k = & - \sum_{j,m} a_{j,m,k}^\dagger [\eta b_{j,m,k} + \xi b_{j,m+1,k}] \\ & + \sum_{j,m}^{BL} V_j \left[a_{j,m,k}^\dagger a_{j,m,k} + b_{j,m,k}^\dagger b_{j,m,k} \right] + \text{H.c.} \\ & - t_\perp \sum_m^{BL} a_{1,m,k}^\dagger b_{2,m,k} + \text{H.c.} \end{aligned} \quad (\text{A1})$$

where η and ξ are defined in the main text.

By multiplying $H_k |\psi_k\rangle = \epsilon_k |\psi_k\rangle$ by $\langle m, l, \mu |$, for a given lattice point (m, l, μ) , where m stands for position, l for layer, and $\mu = A, B$ labels sublattices, one obtains, for the leads where $m < 0$ or $m > p + 1$,

$$\begin{aligned} \epsilon \psi_{m,k}^{A1} &= -\eta \psi_{m,k}^{B1} - \xi \psi_{m+1,k}^{B1} \\ \epsilon \psi_{m,k}^{B1} &= -\eta^* \psi_{m,k}^{A1} - \xi^* \psi_{m-1,k}^{A1}, \end{aligned}$$

with $\psi_{m,k}^{\mu l} = \langle m, \mu, l | \psi_k \rangle$. We rewrite the latter equations in a matrix equation form as

$$\begin{bmatrix} \epsilon & \xi \\ \eta^* & 0 \end{bmatrix} \begin{bmatrix} \psi_{m,k}^{A1} \\ \psi_{m+1,k}^{B1} \end{bmatrix} = - \begin{bmatrix} 0 & \eta \\ \xi^* & \epsilon \end{bmatrix} \begin{bmatrix} \psi_{m-1,k}^{A1} \\ \psi_{m,k}^{B1} \end{bmatrix}, \quad (\text{A2})$$

which is equivalent to Eq. (5).

Similar steps can be taken to build the transfer matrix for the bilayer region where $1 \leq m \leq p$,

$$\begin{aligned} (\epsilon_k - V_1) \psi_{m,k}^{A1} &= -\eta \psi_{m,k}^{B1} - \xi \psi_{m+1,k}^{B1} - t_\perp \psi_{m,k}^{B2} \\ (\epsilon_k - V_1) \psi_{m,k}^{B1} &= -\eta^* \psi_{m,k}^{A1} - \xi^* \psi_{m-1,k}^{A1} \\ (\epsilon_k - V_2) \psi_{m,k}^{A2} &= -\eta \psi_{m,k}^{B2} - \xi \psi_{m+1,k}^{B2} \\ (\epsilon_k - V_2) \psi_{m,k}^{B2} &= -\eta^* \psi_{m,k}^{A2} - \xi^* \psi_{m-1,k}^{A2} - t_\perp \psi_{m,k}^{A1}, \end{aligned}$$

from which we obtain Eq. (7) in matrix form.

By imposing the boundary conditions for setup $1 \rightarrow 1$, and defining $\mathbb{M} = (\mathbb{T}_{BL})^p$, we can re-write Eq. (9) as

$$\begin{bmatrix} \psi_{p,k}^{A1} \\ \psi_{p+1,k}^{B1} \end{bmatrix} = \mathcal{M}_{1 \rightarrow 1} \begin{bmatrix} \psi_{0,k}^{A1} \\ \psi_{1,k}^{B1} \end{bmatrix}, \quad (\text{A3})$$

or equivalently,

$$\Psi_k^1(p+1) = \mathcal{M}_{1 \rightarrow 1} \Psi_k^1(1), \quad (\text{A4})$$

where

$$\mathcal{M}_{1 \rightarrow 1} = \frac{1}{\mathbb{M}_{44}} \begin{bmatrix} \mathbb{M}_{11}\mathbb{M}_{44} - \mathbb{M}_{14}\mathbb{M}_{41} & \mathbb{M}_{12}\mathbb{M}_{44} - \mathbb{M}_{14}\mathbb{M}_{42} \\ \mathbb{M}_{21}\mathbb{M}_{44} - \mathbb{M}_{24}\mathbb{M}_{41} & \mathbb{M}_{22}\mathbb{M}_{44} - \mathbb{M}_{24}\mathbb{M}_{42} \end{bmatrix}.$$

Using the boundary condition for the setup $1 \rightarrow 2$, we obtain, after similar steps,

$$\Psi_k^2(p+1) = \mathcal{M}_{1 \rightarrow 2} \Psi_k^1(1), \quad (\text{A5})$$

where

$$\mathcal{M}_{1 \rightarrow 2} = \frac{1}{\mathbb{M}_{24}} \begin{bmatrix} \mathbb{M}_{24}\mathbb{M}_{31} - \mathbb{M}_{34}\mathbb{M}_{21} & \mathbb{M}_{24}\mathbb{M}_{32} - \mathbb{M}_{34}\mathbb{M}_{22} \\ \mathbb{M}_{24}\mathbb{M}_{41} - \mathbb{M}_{44}\mathbb{M}_{21} & \mathbb{M}_{24}\mathbb{M}_{42} - \mathbb{M}_{44}\mathbb{M}_{22} \end{bmatrix}.$$

The last step is to represent wave amplitudes $\Psi_k^{1(2)}(m)$ in the eigenbasis of the transfer matrix of the leads. The characteristic equation for the eigenvalue problem $\mathbb{T}_L \zeta_k = \lambda \zeta_k$ reads,

$$(\xi_k \eta_k^*) \lambda^2 - (\varepsilon^2 - |\xi_k|^2 - |\eta_k|^2) \lambda + \xi_k^* \eta_k = 0, \quad (\text{A6})$$

yielding two eigenvalues,

$$\lambda_{\pm} = \frac{1}{\xi_k \eta_k^*} \left(\varepsilon^2 - |\xi_k|^2 - |\eta_k|^2 \pm \sqrt{(\varepsilon^2 - \delta_+^2)(\varepsilon^2 - \delta_-^2)} \right), \quad (\text{A7})$$

where $\delta_{\pm} = |\xi_k| \pm |\eta_k|$, corresponding to the normalized eigenvectors

$$\zeta_k^{\pm} = \frac{1}{\sqrt{2}} \begin{pmatrix} 1 \\ \frac{-\varepsilon}{\xi_k^* + \eta_k^* \lambda_{\pm}} \end{pmatrix}. \quad (\text{A8})$$

A mode with positive (negative) group velocity is considered to be the right-moving(+) (left-moving(-)) mode. Recalling that in the leads $|\lambda| = 1$ and using Bloch theorem for the Pristine graphene $\lambda = e^{iq(k, \varepsilon)}$, where $q(k, \varepsilon)$ is the conjugate momentum in \mathbf{a}_1 (propagating) direction, and plugging the latter expression into Eq. (A6) we obtain the mode group velocity in the propagating direction as:

$$v_g = \frac{d\varepsilon}{dq} = \frac{-1}{\varepsilon} \text{Im}(\xi_k \eta_k^* \lambda(k, \varepsilon)) \quad (\text{A9})$$

-
- [1] K. S. Novoselov, *Science* **306**, 666 (2004), arXiv:0410550 [cond-mat].
- [2] A. K. Geim and K. S. Novoselov, *Nature Materials* **6**, 183 (2007), arXiv:0702595v1 [cond-mat].
- [3] A. K. Geim, "Graphene: Status and prospects," (2009), arXiv:0906.3799.
- [4] A. H. Castro Neto, N. M. R. Peres, K. S. Novoselov, A. K. Geim, and F. Guinea, *Reviews of Modern Physics* **81**, 109 (2009), arXiv:0709.1163v2.
- [5] P. Avouris, *Nano Letters* **10**, 4285 (2010).
- [6] F. Xia, H. Yan, and P. Avouris, *Proceedings of the IEEE* **101**, 1717 (2013).
- [7] H. Chen, M. B. Müller, K. J. Gilmore, G. G. Wallace, and D. Li, *Advanced Materials* **20**, 3557 (2008).
- [8] G. Eda and M. Chhowalla, *Nano Letters* **9**, 814 (2009).
- [9] T. Georgiou, R. Jalil, B. D. Belle, L. Britnell, R. V. Gorbachev, S. V. Morozov, Y.-J. Kim, A. Gholinia, S. J. Haigh, O. Makarovskiy, L. Eaves, L. A. Ponomarenko, A. K. Geim, K. S. Novoselov, and A. Mishchenko, *Nature Nanotechnology* **8**, 100 (2012), arXiv:1211.5090.
- [10] H. Jang, Y. J. Park, X. Chen, T. Das, M. S. Kim, and J. H. Ahn, *Advanced Materials* **28**, 4184 (2016).
- [11] J. P. Llinas, A. Fairbrother, G. Borin Barin, W. Shi, K. Lee, S. Wu, B. Yong Choi, R. Braganza, J. Lear, N. Kau, W. Choi, C. Chen, Z. Pedramrazi, T. Dumslaff, A. Narita, X. Feng, K. Müllen, F. Fischer, A. Zettl, P. Ruffieux, E. Yablonovitch, M. Crommie, R. Fasel, and J. Bokor, *Nature Communications* **8**, 8 (2017), arXiv:1605.06730.
- [12] F. Schwierz, *Nature Nanotech* **5**, 487 (2010), arXiv:NIHMS150003.
- [13] Y.-W. Son, M. L. Cohen, and S. G. Louie, *Physical Review Letters* **97** (2006), 10.1103/PhysRevLett.97.216803, arXiv:0611602 [cond-mat].
- [14] M. Y. Han, B. Ozyilmaz, Y. Zhang, and P. Kim, *Physical review letters* **98**, 206805 (2007), arXiv:0702511 [cond-mat].
- [15] Z. C. Å, Y.-m. Lin, M. J. Rooks, and P. Avouris, *Physica E* **40**, 228 (2007), arXiv:0701599 [cond-mat].
- [16] K. Wakabayashi, Y. Takane, M. Yamamoto, and M. Sigrist, *New Journal of Physics* **11** (2009), 10.1088/1367-2630/11/9/095016, arXiv:arXiv:0907.5243v1.
- [17] S. Y. Zhou, G. H. Gweon, A. V. Fedorov, P. N. First, W. A. De Heer, D. H. Lee, F. Guinea, A. H. Castro Neto, and A. Lanzara, *Nat. Mater.* **6**, 770 (2007).
- [18] E. V. Castro, K. S. Novoselov, S. V. Morozov, N. M. R. Peres, J. M. B. L. Dos Santos, J. Nilsson, F. Guinea, A. K. Geim, and A. H. C. Neto, *Physical Review Letters* **99** (2007), 10.1103/PhysRevLett.99.216802, arXiv:0611342 [cond-mat].
- [19] E. V. Castro, N. M. R. Peres, J. M. B. L. Dos Santos, F. Guinea, and A. H. C. Neto, *Journal of Physics: Conference Series* **129** (2008), 10.1088/1742-6596/129/1/012002, arXiv:1004.5079.
- [20] E. V. Castro, K. S. Novoselov, S. V. Morozov, N. M. R. Peres, J. M. B. Lopes Dos Santos, J. Nilsson, F. Guinea, A. K. Geim, and A. H. Castro Neto, *Journal of Physics Condensed Matter* **22** (2010), 10.1088/0953-8984/22/17/175503, arXiv:0807.3348.
- [21] Y. Zhang, T.-T. Tang, C. Girit, Z. Hao, M. C. Martin, A. Zettl, M. F. Crommie, Y. R. Shen, and F. Wang, *Nature* **459**, 820 (2009).
- [22] E. McCann and M. Koshino, *Rep. Prog. Phys.* **76**, 56503 (2013).
- [23] G. Li, A. Luican, J. M. B. Lopes Dos Santos, A. H. Castro Neto, A. Reina, J. Kong, and E. Y. Andrei, *Nature Phys.* **6**, 109 (2010).
- [24] A. Luican, G. Li, A. Reina, J. Kong, R. R. Nair, K. S. Novoselov, A. K. Geim, and E. Y. Andrei, *Phys. Rev. Lett.* **106**, 126802 (2011).
- [25] B. Amorim, *Physical Review B* **97**, 165414 (2018), arXiv:1711.02499.
- [26] Y. Cao, V. Fatemi, S. Fang, K. Watanabe, T. Taniguchi, E. Kaxiras, and P. Jarillo-Herrero, *Nature* **556**, 43 (2018), arXiv:1803.02342.
- [27] Y. Cao, V. Fatemi, A. Demir, S. Fang, S. L. Tomarken, J. Y. Luo, J. D. Sanchez-Yamagishi, K. Watanabe, T. Taniguchi, E. Kaxiras, R. C. Ashoori, and P. Jarillo-Herrero, *Nature* **556**, 80 (2018), arXiv:1802.00553.
- [28] A. Mishchenko, J. S. Tu, Y. Cao, R. V. Gorbachev, J. R. Wallbank, M. T. Greenaway, V. E. Morozov, S. V. Morozov, M. J. Zhu, S. L. Wong, F. Withers, C. R. Woods, Y. J. Kim, K. Watanabe, T. Taniguchi, E. E. Vdovin, O. Makarovskiy, T. M. Fromhold, V. I. Falko, A. K. Geim, L. Eaves, and K. S. Novoselov, *Nature Nanotechnology* **9**, 808 (2014).
- [29] L. Britnell, R. V. Gorbachev, R. Jalil, B. D. Belle, F. Schedin, A. Mishchenko, T. Georgiou, M. I. Katsnelson, L. Eaves, S. V. Morozov, N. M. R. Peres, J. Leist, A. K. Geim, K. S. Novoselov, and L. A. Ponomarenko, *Science* **335**, 947 (2012), arXiv:1112.4999.

- [30] L. Britnell, R. V. Gorbachev, R. Jalil, B. D. Belle, F. Schedin, M. I. Katsnelson, L. Eaves, S. V. Morozov, A. S. Mayorov, N. M. R. Peres, and Others, *Nano Letters* **12**, 1707 (2012).
- [31] B. Amorim, R. M. Ribeiro, and N. M. R. Peres, *Physical Review B* **93**, 235403 (2016), arXiv:1603.04446.
- [32] F. Chen, H. Ilatikhameneh, Y. Tan, G. Klimeck, and R. Rahman, *IEEE Transactions on Electron Devices* **65**, 3065 (2018), arXiv:1711.01832.
- [33] J. Li, K. Wang, K. J. McFaul, Z. Zern, Y. Ren, K. Watanabe, T. Taniguchi, Z. Qiao, and J. Zhu, *Nature Nanotechnology* (2016).
- [34] I. Martin, Y. M. Blanter, and A. F. Morpurgo, *Physical Review Letters* **100** (2008), 10.1103/PhysRevLett.100.036804, arXiv:0709.3522.
- [35] M. Koshino, *Physical Review B - Condensed Matter and Materials Physics* **88**, 115409 (2013), arXiv:1307.3421.
- [36] I. Snyman and C. W. Beenakker, *Physical Review B - Condensed Matter and Materials Physics* **75** (2007), 10.1103/PhysRevB.75.045322, arXiv:0609243 [cond-mat].
- [37] J. Nilsson, A. H. Castro Neto, F. Guinea, and N. M. R. Peres, *Physical Review B - Condensed Matter and Materials Physics* **76**, 165416 (2007), arXiv:0607343 [cond-mat].
- [38] B. A. Bernevig, T. L. Hughes, and S. C. Zhang, *Science* **314**, 1757 (2006), arXiv:arXiv:1308.5367.
- [39] T. Nakanishi, M. Koshino, and T. Ando, *Physical Review B - Condensed Matter and Materials Physics* **82**, 125428 (2010), arXiv:1008.4450.
- [40] J. W. González, H. Santos, M. Pacheco, L. Chico, and L. Brey, *Physical Review B - Condensed Matter and Materials Physics* **81**, 195406 (2010), arXiv:1002.3573.
- [41] J. W. González, H. Santos, E. Prada, L. Brey, and L. Chico, *Phys. Rev. B* **83**, 205402 (2011).
- [42] K.-L. Chu, Z.-B. Wang, J. Zhou, and H. Jiang, *Chinese Phys. B* **26**, 067202 (2017).
- [43] S. Datta, *Quantum transport: atom to transistor* (Cambridge university press, 2005).
- [44] M. Büttiker, Y. Imry, R. Landauer, and S. Pinhas, *Physical Review B* **31**, 6207 (1985).